Electrostatically Actuated Thin-Shell Space Structures

Fabien Royer*, John Z. Zhang [†], Kaleb D. Overby[‡], Elizabeth Y. Zhu[§], Harsh G. Bhundiya [¶],
Jeffrey H. Lang[‖] and Zachary C. Cordero**
Massachusetts Institute of Technology, Cambridge, MA, 02139

We present a novel electrostatic thin-shell structure concept capable of actively controlling the shape of large area systems with minimal mass overhead and complexity. It consists of an assembly of collapsible thin-shell cells for which the cross-section follows the classical Collapsible Tubular Mast (CTM) architecture. Two conductive electrodes are added to the top and bottom flanges of the cell. An electrostatic force develops between top and bottom electrodes upon voltage application, which flattens the cross-section and causes the cell to expand longitudinally. When multiple layers of these cells are bonded to each other, the controlled differential expansion of each layer can be harnessed to cause global bending.

Nomenclature

α_0 = initial cross-section opening angle
r_0 = initial cross-section radius
l_0 = initial width of the structure
w_e = electrode width
h = cross-section deployed height
N_i = number of honeycomb rows
N_j = number of honeycomb columns
T = electrode surface traction
d_i = distance between electrode slices
ϵ_r = relative permittivity of air
ϵ_0 = absolute permittivity of vacuum
ϵ_p = relative permittivity of polyimide
t_p = thickness of polyimide layer
V = voltage applied between electrodes

I. Introduction

Large spacecraft architectures will be paramount in addressing major societal issues and fostering the next generation of robotics and human space exploration. For instance, large radiometry satellites can dramatically augment our climate modelling capabilities and improve our forecasting of natural disasters [1]. In the energy sector, space solar power satellites can collect sunlight continuously throughout the day, convert it into microwaves and send it directly where needed on Earth, hence solving current issues in storing and transferring renewable energies across the globe [2]. Similar large space architectures can be leveraged to enable deep-space electric propulsion and the non-nuclear exploration of the outer solar system [3], as well as large infrastructures and habitats on the Moon and on Mars. Besides very large space structures, lighter and larger apertures can be integrated in small satellites, paving the way for highly capable mega-constellations and new applications [4]. Finally, these structures will be key enablers of future space telescopes [5].

---

*Postdoctoral associate, MIT AeroAstro, 77 Massachusetts Ave, Cambridge MA 02139.
[†]PhD student, MIT Mechanical Engineering, 77 Massachusetts Ave, Cambridge MA 02139.
[‡]Master student, MIT AeroAstro, 77 Massachusetts Ave, Cambridge MA 02139.
[§]Undergraduate student, MIT AeroAstro, 77 Massachusetts Ave, Cambridge MA 02139.
[¶]PhD student, MIT AeroAstro, 77 Massachusetts Ave, Cambridge MA 02139.
[‖]Vitesse Professor of Electrical Engineering, MIT EECS, 77 Massachusetts Ave, Cambridge MA 02139.
**Boeing Assistant Professor of Aeronautics and Astronautics, MIT AeroAstro, 77 Massachusetts Ave, Cambridge MA 02139.

However, keeping a high surface accuracy for large aperture systems is extremely challenging, and the size of space structures was hitherto limited by disturbances on orbit [6], confining existing flight systems to diameters measuring only a few tens of meters [7]. The need for active space structures to compensate for the effect of disturbances (thermal distortions, inertial loads, vibrations, gravity gradient, solar pressure) has been identified for a long time [8]. Active surface control has been implemented in telescopes [9], further pushing the limit of aperture size. However these control strategies require large and heavy actuators, and scaling these approaches to extremely large space structures ($D > 50$ m) becomes extremely difficult. One solution consists in embedding active materials into lightweight structural architectures. Such an approach was used to create ultrathin deformable mirrors [10].

Recent advances in soft robotics focused on the development of extremely space and mass efficient actuators. One such example is artificial muscles. Multiple concepts have been investigated using temperature sensitive polymers, pneumatic and chemical actuation and other physical processes. However, most of these solutions cannot be translated directly to space structures since they are extremely sensitive to the environment in which they are operated. However, electrostatic actuation appears to be a particularly promising candidate, as it can be easily integrated into flexible structures with very minimal mass overhead. Such actuators were first developed in MEMS[11] at very small scales. More recent concepts used networks of stacked electrostatic actuators[12] and electrostatic membrane cells in series[13] in larger scale systems, and are able to produce large linear motions. A further improved version of the larger scale actuators used electrostatic ribbons with liquid dielectric to produce even larger deflections and linear contractions. However, even if these systems are lightweight, they are not stiff in bending and therefore are not adapted to large load-bearing and self-supporting structures. In addition, these systems are focused on linear actuation.

Electrostatic actuation has been investigated to control the shape of large space antennas [14, 15] and flexible mirrors [16] but these concepts require a stiff command surface electrode which is challenging to integrate in lightweight deployable structures. Inspired by advances in soft robotics and by pioneer research on electrostatic actuation of large membranes, this paper introduces a novel thin-shell electrostatic structure concept to actively control the shape of large space systems. It extends the use of electrostatic soft actuators to bending stiff structures, and it is able to produce bending deformations in large scale structures. The structure, which resembles an honeycomb, features multiple cells on which conductive electrodes are patterned. When an electric field is applied between electrodes, an electrostatic force develops and the cell is pinched which in turns generates linear expansion along the cell longitudinal direction. When these cells are arranged into layers, differential expansion causes bending deformations, similar to previous robotic surface concepts [17]. These honeycombs can then be assembled into more complex systems, such as lightweight planar lattices [18], which can form large aperture systems capable of adjusting their shape in real time on orbit. These structures can be fully flattened and coiled into a tight volume, thus offering great opportunities to integrate actuation into deployable space structures. They also offer a very lightweight and scalable alternative to electroactive polymer actuators [?].

The paper is organized as follows. Section II introduces the thin-shell electrostatic structure concept. A simulation framework capable of modeling the complex non-linear behavior of these structures is then presented in Section III, and the manufacturing and experimental setup used to test these structures is described. The finite element framework is used in Section IV.A to conduct parametric studies on single electrostatic cells and bilayer structures, and highlight their actuation capabilities (expansion, force, rotation and reaction moment). Section V synthesises bending actuation experiments for two electrode architectures and two geometries, and Section VI describes how to extend the use of these structures to large scale shape morphing lattices. Finally VII concludes the paper and offers insights into future research avenues.

II. Concept

A thin-shell honeycomb-like structure is formed using thin-ply fiber composites. The shell cross-section follows the classical lenticular shape, found in Collapsible Tubular Masts (CTM)[19], which can be fully collapsed into a thin sheet of material. When fully deployed, a cell has width l_0 and height h_0. When the cross-section is pinched, its height decreased to $h < h_0$, resulting in an increase in width $l > l_0$ to conserve the flange arclength. This expansion mechanism is controlled using electrostatic actuation. Conductive electrodes attached to the cell top and bottom flanges are connected to a high voltage power supply, and an electrostatic force is created upon voltage application. The cross-section pinching (i.e height variation) and therefore the cell expansion, can be controlled in real time by varying the applied voltage. Cells are arranged into layers and differential expansion is harnessed to produce large bending deformations. The concept is illustrated in Figure 1a and the geometric parameters defining the cell cross-sections are shown in Figure 1b. Two types of electrode configuration are considered here. In the parallel electrode scheme, shown

on the left in Figure 1a, electrodes are spanning the flat top and bottom sections of the cell, whereas zipper electrodes are spanning the entire cell cross-section, as shown on the right in Figure 1a.
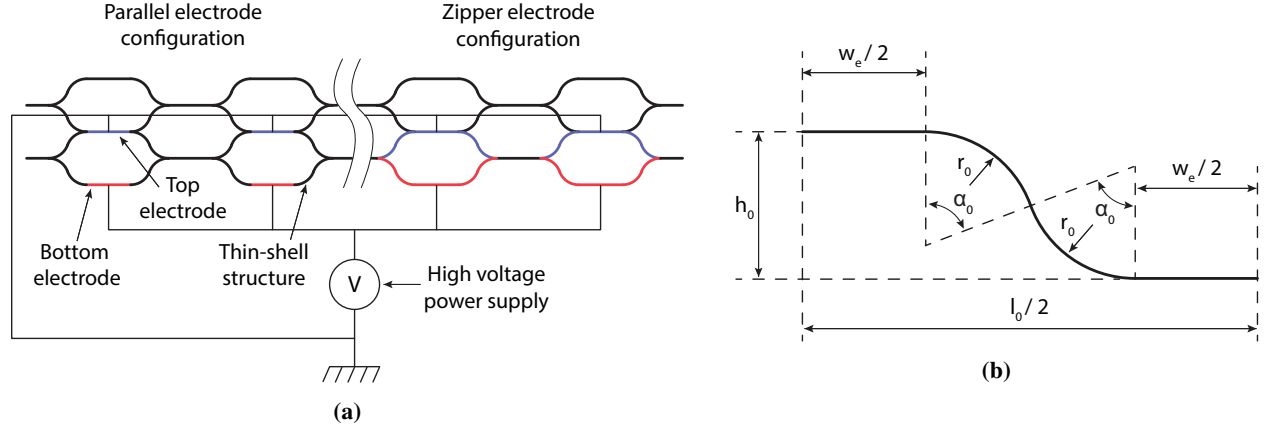

Fig. 1 (a) Electrostatic honeycomb concept description, highlighting the two electrode configurations, parallel and zipper. (b) Cross-section geometric parameters. Only one quarter of the cross-section is shown.

III. Methods

A. Finite element modeling

A parametric finite element framework is used to assess the actuation capabilities of a single cell, a two-cell system, as well as full honeycomb lattice. It uses the finite element software Abaqus and its Python and Fortran scripting capabilities. The model geometry is generated using a Python script which takes as inputs the cross-section radius and opening angle, as well as the number of lattice rows, columns and layers. The structure is made of a 2-ply laminate, modelled with the Abaqus composite section module. The innermost ply is made of a 55 μm thick unidirectional glass fiber reinforced plastic (GFRP, S2/ Patz PMT-F7) on which a 57 μm thick polyimide (DuPont Kapton) layer is bonded. An additional layer, composed of 50 μm thick copper foil is added to the laminate is sandwiched between the glass fiber and polyimide plies in the electrode region. The cross-section closes in the web regions, where the top and bottom flange laminates are stacked. The material properties used in the finite element model are summarized in Table 1. The structure is meshed with rectangular reduced integration shell elements (S4R), with an edge seed spacing of 0.7 mm.

	E_1 (GPa)	E_2 (GPa)	G_{12} (GPa)	ν_{12}	t (μ m
GFRP	55.0	5.5	6.4	0.26	55.2
Copper	130.0	-	-	0.36	50.8
Polyimide	2.8	-	-	0.34	57.1

Table 1   Material properties used in the finite element model.

The electrostatic force is modelled as a set of surface tractions along the y direction. Each electrode is discretized into rows of elements (constant x-coordinate) on which a uniform traction magnitude is defined. For row i with centroid coordinate x_i, the traction magnitude is computed as

$$T(x_i) = \frac{1}{2}\epsilon_0\epsilon_r \left(\frac{V}{d_i + 2\frac{t_p}{\epsilon_p}}\right)^2 \tag{1}$$

where ϵ_0 is the permittivity of vacuum, ϵ_r is the relative permittivity of air, ϵ_p is the relative permittivity of polyimide (3.4), t_p is the thickness of the polyimide layer, V is the applied voltage, and d_i is the distance between the centroids of row i and row i' directly facing on the opposite electrode, see Figure 2. At each analysis increment, the voltage is increased, and for a given row i, the coordinates of nodes N1i, N2i, N1i' and N2i' are extracted using Sensors (from the

3

field output request in Abaqus). These coordinates are then fed to a UAMP Fortran subroutine which computes d_i and updates the traction magnitude for the given electrode row. The analysis is geometrically non-linear since the traction magnitude depends on the deformed geometry and its direction follows the rotation of the electrode rows.
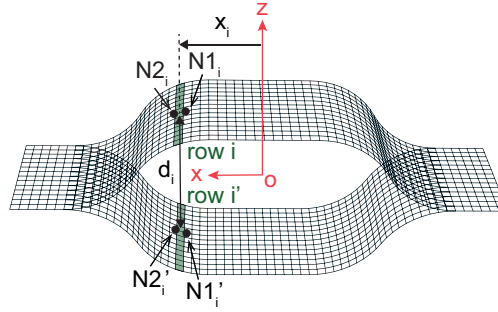

Fig. 2   Description of the electrode slicing into rows and nodes used for the traction computation.

B. Manufacturing

To fabricate the structure, we employ a novel silicone molding process [20, 21] which enables the accurate manufacturing of thin-ply composites without the need for an autoclave. It uses aluminum cages which enclosed silicone rubber parts whose shape follows the desired cross-section. During curing, the metal cages keep the enclosed volume constant, and the incompressibility of the silicone rubber prevents any shape distortions. In addition, the silicone thermal expansion induces a high pressure into the mold, comparable to magnitudes used in an autoclave curing process.

The manufacturing process follows several steps. First, 3D printed mold negatives are used to form the silicone rubber into the desired cross-section shape. Figure 3a shows the 3D printed mold negative used to create the blue silicone pieces which are then enclosed in aluminum cages. The GFRP, polyimide and electrode plies are then laminated into a strip of material which is then laid into the silicone mold. Male silicone plugs are placed inside the mold cavities and an additional strip of material is added to form the second half of the closed cross-section, as shown in Figure 3b. Finally, the mold is then fully enclosed into the metal caging, placed into an oven, and cured for seven hours. For these specific mold geometry, the cure cycle is longer than prescribed by the resin manufacturer [22] to accommodate for the high thermal insulation silicone provides to the laminates. The structures obtained using this process are shown in Section V.
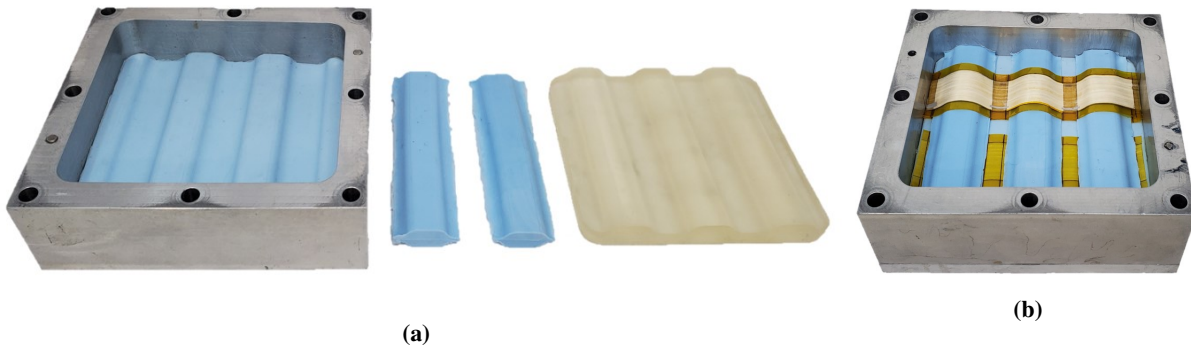

(a)

(b)

Fig. 3   (a) (from left to right) 3D printed mold negative used to create the male silicone plugs and female silicone pieces. (b) The male silicone plugs are added to the mold and cover the bottom laminate, and a laminate is added on top of the plugs to close the cross-section.

C. Experiment

A set of experiments is conducted to assess the actuation capabilities of bilayer electrostatic thin-shell structures. The experimental setup is illustrated in Figure 4. The extremities of the structures are glued into MDF end caps, which ensures a stiff coupling between top and bottom layers. These caps are sitting on cylindrical low friction supports, which approximates simply supported boundary conditions. A small cantilever strip is glued on the top electrode of the central bilayer, and serves as a target for a laser displacement sensor which tracks the central deflection of the neutral axis. An FPGA controls a high voltage power supply (Analog Technologies Inc) which can deliver a voltage between electrodes up to 20 kV. The actual applied voltage and displacement data is retrieved by the FPGA and tracked in real time through a custom Labview program.
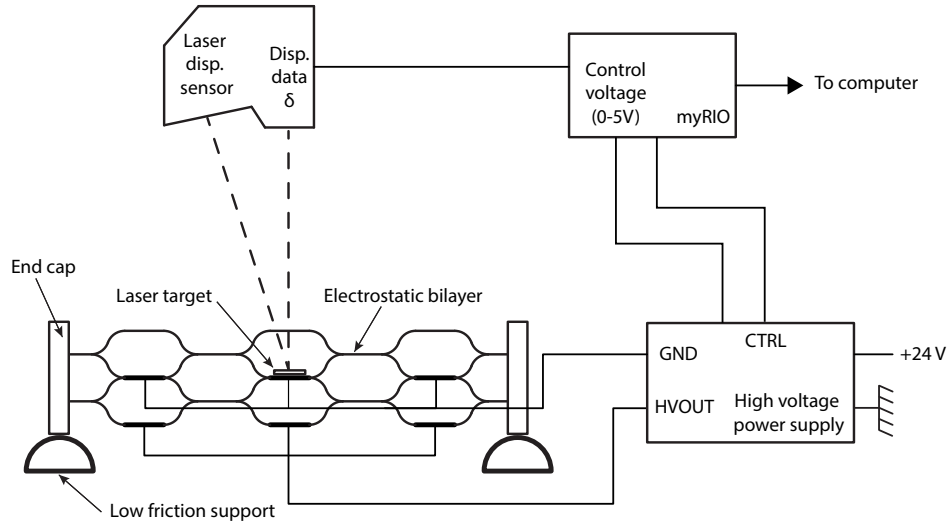

Fig. 4   Schematic of the experimental setup used to test the bending deflection of simply supported electrostatic structures.

IV. Results

A. Parametric study

Two types of analyses are considered here: expansion and bending. Only parallel electrodes are considered in the following parametric study. The expansion analysis, illustrated in Figure 5a, considers a single cell. The electrostatic surface traction is applied to the top and bottom electrodes, and the two sides edges are rigidly coupled to two reference points, on which boundary conditions are applied. To assess the maximum axial linear expansion, and maximum axial force the cell can generate, we consider two types of boundary conditions. The first boundary condition scheme (simply supported, U_x free) has the right reference point (RP1) fully clamped while the left reference point (RP2) is only allowed to translate in the x direction. The displacement of RP1 in the x direction is used to compute the cell expansion. In the second boundary condition scheme (clamped, $U_x = 0$), RP2 is fully clamped and the reaction force in the x direction is extracted.

In the bending analysis, illustrated in Figure 5b, two unit cells are considered. They are bonded on top of each other using a tie constraint on their flat flange surface. The sides edges of both top and bottom cells are rigidly coupled to two reference points (RP1 and RP2), on which boundary conditions are applied. Two boundary condition schemes are considered. In both boundary condition schemes, the two reference points are allowed to rotate around the z-axis, while RP2 is free to translate along the x-direction. In the first boundary condition scheme, RP1 and RP2 are left unconstrained and the rotation of RP2 around the z axis is extracted. In the second boundary condition scheme, both reference points are clamped and the reaction moment at RP2 is retrieved.
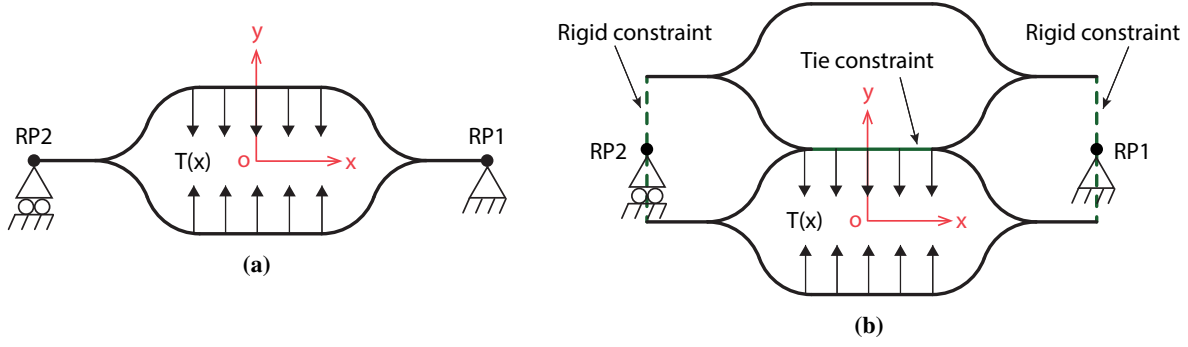
Fig. 5   Description of the (a) expansion analysis and (b) bending analysis.

1. Expansion mode

In this section, we present the results of the expansion analysis for the simply supported and clamped boundary conditions, and for various cell geometries. For the rest of the paper, the cell depth is $b = 25$ mm and the flat electrode section width is $w_e = 13$ mm. The cross-section opening angle α_0 is varied between 5 deg and 30 deg, and the cross-section height h_0 between 0.5 mm and 3.25 mm. The electromechanical system formed by the shell structure and the electrodes is highly nonlinear. The electrostatic force increases quadratically as the shell deforms and the gap between electrode narrows. Since the structural stiffness in the y direction is approximately linear, the cross-section vertical displacement increases quadratically when the voltage increases linearly. At a critical voltage, the system destabilizes, and the displacement vs voltage curve exhibits a vertical tangent. At this point, the structure undergoes a snap-through referred to as pull-in instability, and the two electrodes come into contact. The instability occurs when the voltage reaches the pull-in voltage V_p. A more complete discussion of the pull-in instability in electromechanical systems is available in [15]. Note that for the scope of this paper, the maximum voltage is set to 20 kV. Figure 6a shows expansion vs voltage characteristics, as a function of the cross-section height and opening angle. The end point of the characteristic is used as an approximation of the pull-in point. In reality, pull-in occurs when the tangent to the curve is strictly vertical, and therefore at slightly higher voltages. We observe a clustering of expansion characteristic for a given value of opening angle. For $\alpha_0 = 30$ deg and $h_0 = 2.0$ mm and $h_0 = 3.0$ mm, the expansion characteristics reach the maximum voltage before pull-in occurs, and expansion is limited by the system's electrical capabilities rather than by instabilities. Reaction force characteristics are presented in Figure 6b. We notice that there is no clustering of curves based on the opening angle and they are rather ordered by cross-section height. The parametric study presented next focuses on using the electrostatic honeycomb before pull-in to allows for a continuous and smooth actuation. Therefore, this preliminary study does not intend to analyze the behavior of the cell past its instability. However, operating the cells beyond pull-in can be utilized to achieve large deformations, and as a locking mechanism to achieve high load bearing capabilities on demand. The unstable behavior of the cells beyond pull-in will be investigated in future work. From a practical consideration, the voltage may be limited by the dielectric breakdown of the air between electrodes, and a coating with high dielectric constant may be added to the electrode surface to minimize the risk of arcing. This practical considerations are discussed in Section V.
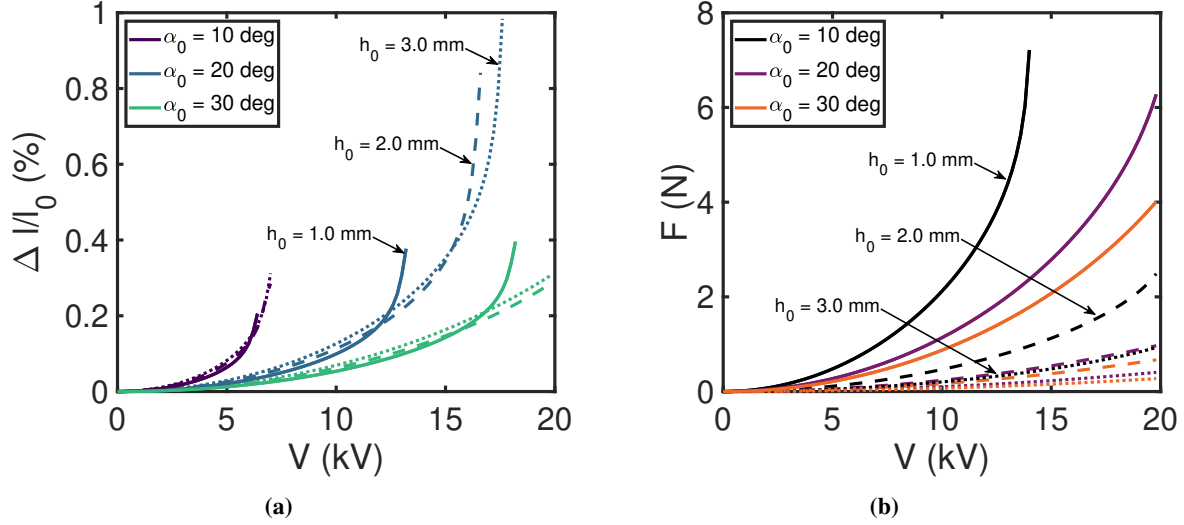
Fig. 6 **(a) Cell expansion and (b) reaction force along the x axis as a function of applied voltage, for various values of cross-section height and opening angle.**

Figure 7a shows the evolution of the axial cell expansion at pull-in, for the simply supported boundary conditions. In addition, contours of equal pull-in voltage are overlaid in white dashed lines. The maximum pull-in voltage is achieved for higher values of height and opening angle, which correspond to stiffer cross-sections in the y direction (flattening stiffness). Above the solid white line in Figure 7a, the maximum voltage is reached before pull-in occurs. The highest values of expansion are achieved for $\alpha_0 = 20$ deg and monotonically increase with the cross-section height. For $\alpha_0 = 20$ deg and $h_0 = 3.25$ mm, the maximum value of expansion is achieved and is around 1%. For larger values of opening angles, the ratio between the flange arclength and the initial cell length increases, potentially providing more actuation capabilities. However, the distance between electrodes increases and the electric field strength is weaker for the same applied voltage.

The undeformed and deformed cell shapes for $h_0 = 3.25$ mm and $\alpha_0 = 20$ deg are shown in Figure 7c, with a color map of the vertical cross-section displacement. At pull-in and for this specific geometry, the cross-section height decreases by 85 %. Note that the deformed shape features both flattening of the curved flanges and bending of the electrodes. While the curve flange flattening provides positive expansion, the bending of the electrodes reduces the cell actuation capabilities. It suggests that the actuation efficiency of parallel electrode cells could be further improved by increasing the local bending stiffness in the electrode region.

Figure 7c shows the evolution of the axial reaction force and voltage at pull-in, for the clamped boundary conditions. For a given h_0 and α_0, the pull-in voltage more than doubles when the simply supported boundary conditions are replaced by the clamped boundary conditions, due to the increase in flattening stiffness for all geometries. The reaction force increases as the cross-section height decreases, since the reduction in initial distance between the electrodes causes a quadratic increase in electric field. At very low h_0, the reaction force is highest for larger α_0. This range of geometric parameters corresponds to higher values of bending stiffness for the curved flanges, and the electrostatic force is transferred to the cell edges with minimal deformations of these flanges. The maximum value of reaction force is reached for $h_0 = 0.5$ mm and $\alpha_0 = 30$ deg, and is around 15 N. However, when h_0 increases, the region of highest reaction force shifts to lower values of opening angles. Note that the region for which the maximum voltage is reached before pull-in is greatly extended for this boundary condition scheme.

The undeformed and deformed cell shapes for $h_0 = 0.75$ mm and $\alpha_0 = 20$ deg are shown in Figure 7d, with a color map of the vertical cross-section displacement. At pull-in and for this specific geometry, the cross-section height decreases by 52 %. Like in the free expansion case, the deformed shape features both flattening of the curved flanges and bending of the electrodes.
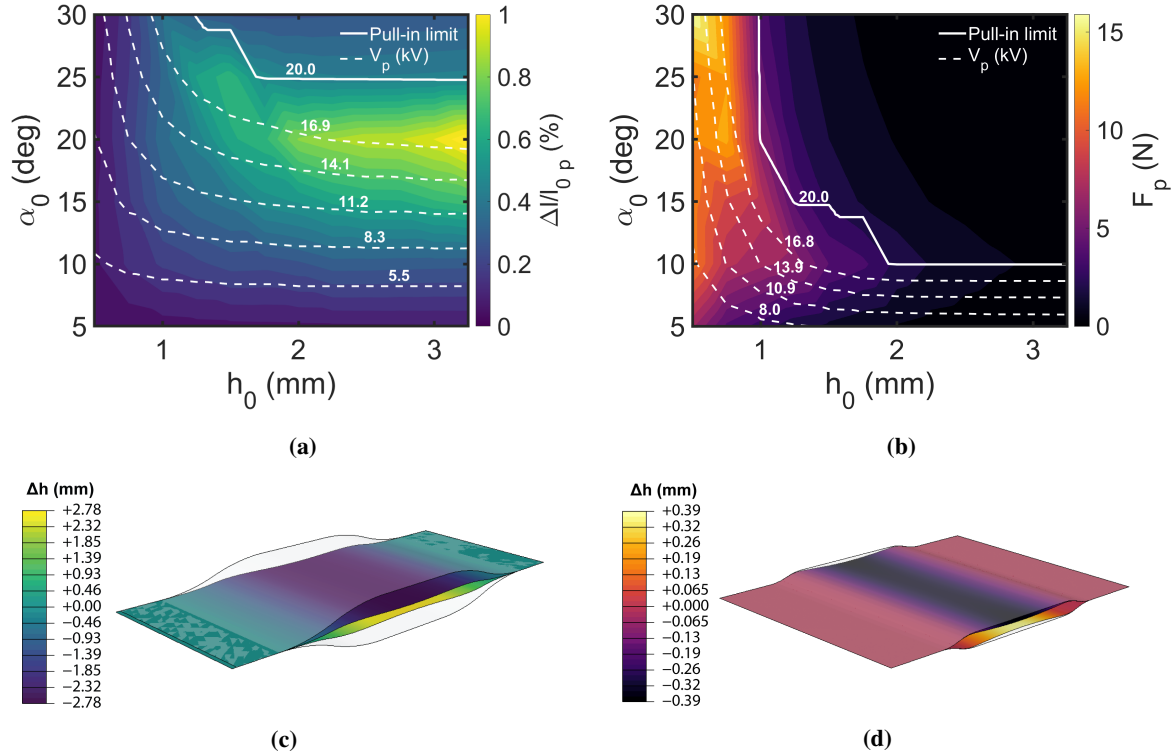
7

(a)   **(b)**

(c)   **(d)**

Fig. 7 **(a) Contour plot of axial cell expansion and pull-in voltage as a function of cross-section height and opening angle, for the simply supported boundary conditions. (b) Contour plot of axial reaction force and pull-in voltage as a function of cross-section height and opening angle, for the clamped boundary conditions. Unreformed and deformed cell for (c) $h_0 = 3.25$ mm and $\alpha_0 = 20$ deg for the simply supported boundary conditions and for (d) $h_0 = 0.75$ mm and $\alpha_0 = 20$ deg for the clamped boundary conditions.**

2. Bending mode

In this section, we present the results of the bending analysis for the simply supported and clamped boundary conditions, and for various cell geometries. The range of geometric parameters considered is the same as for the expansion analysis, and both top and bottom cells are identical. A contour map of the bilayer pull-in rotation and pull-in voltage is shown in Figure 8a. We notice that even if the shape of the voltage contours is qualitatively similar to what is found in the expansion analysis, the values of pull-in voltages increase. The region of no pull-in extends further into lower values of opening angles. These observations are consistent with the increase in top electrode bending stiffness which are caused by the doubling of thickness at the interface between the two cells. Similarly, the region of high bending rotation is found at lower values of opening angles and the rotation magnitude is maximal for $\alpha_0 = 15$ deg. The two local minima of bending rotations are found for $h_0 = 2.25$ mm and $h_0 = 2.75$ mm, with a rotation magnitude close to 4 deg. Even if increasing h_0 leads to higher values of bottom cell expansion, and therefore larger differential expansion between the two layers, it also increases the overall height of the structure which increases its bending stiffness. The competition between these two effects explains that the rotation maxima are not found for $h_0 > 2.75$ mm.

The undeformed and deformed bilayer shapes for $h_0 = 2.75$ mm and $\alpha_0 = 15$ deg is shown in Figure 8c, with a color map of the vertical cross-section displacement. The bottom cell height reduces and the cell expends when the voltage is applied, but local bending deformations localizes on the bottom electrode, since the top electrode thickness is no doubles compared to the single cell configuration. The flattening and axial expansion of the actuated cell causes the height of the top cell to increase, and the cell to contract along the x-axis. The difference in axial expansion between the two cells causes bending.In addition, the bilayer neutral axis shifts upward during the deformation process.

Figure 8c shows the evolution of the reaction moment and the voltage at pull-in, for the clamped boundary conditions. Similarly to the simply-supported boundary conditions analysis, the pull-in voltage increases overall and the high values of reaction moment are shifted to lower opening angles. A maximum reaction moment of 8.9 Nmm is found for

8

$h_0 = 0.75$ mm and $\alpha_0 = 20$ deg. The deformed shape for this specific geometry is shown in Figure 8d, and highlights the localization of deformation (local bending) on the bottom electrode of the actuated cell. Note that the bilayer is shown upside-down in Figure 8d for ease of visualization.
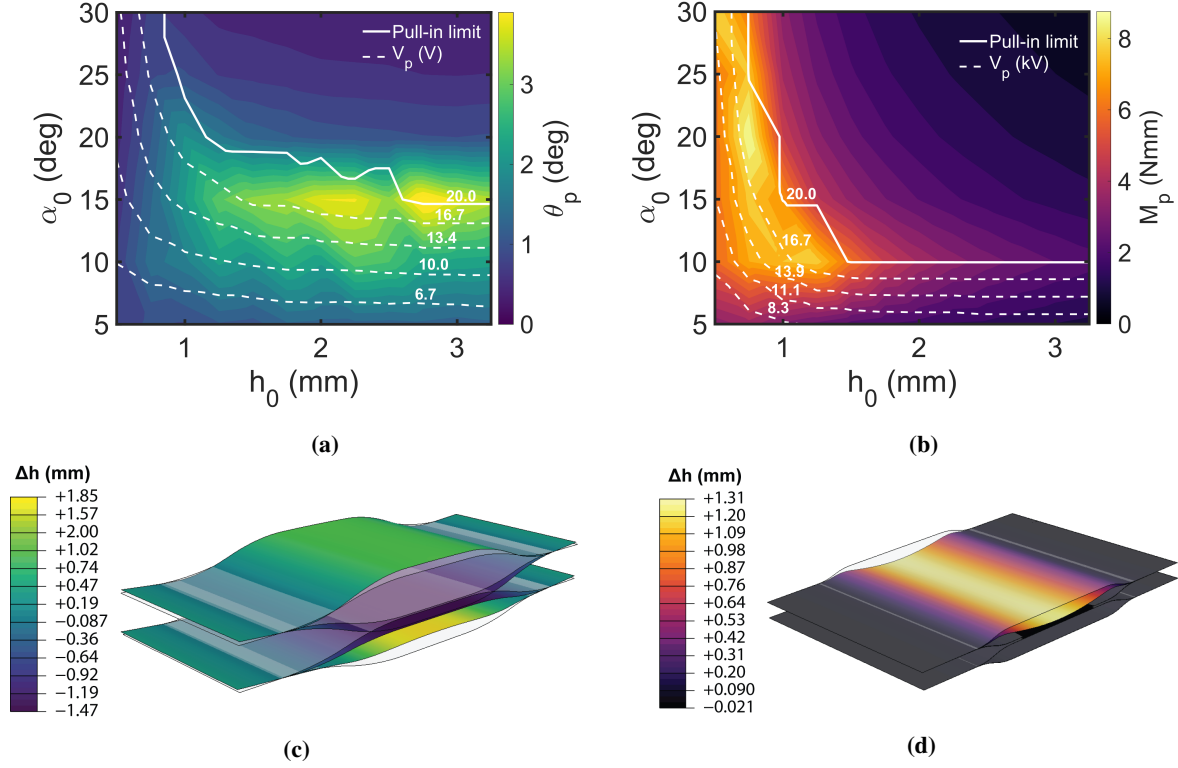

(a)

(b)

(c)

(d)

Fig. 8 (a) Contour plot of end rotation and pull-in voltage as a function of cross-section height and opening angle, for the simply supported boundary conditions. (b) Contour plot of reaction moment and pull-in voltage as a function of cross-section height and opening angle, for the clamped boundary conditions. Unreformed and deformed bilayer shapes for (c) $h_0 = 2.75$ mm and $\alpha_0 = 15$ deg for the simply supported boundary conditions and for (d) $h_0 = 0.75$ mm and $\alpha_0 = 20$ deg for the clamped boundary conditions.

V. Experimental Validation

A series of experiments are conducted on thin-shell electrostatic bilayers, using the setup described in Section III.A. We first focus on structures which feature parallel electrodes, i.e. the electrodes are only spanning the flat top and bottom sections of the cells. 8 prototypes are manufactured. They feature 3 cells per layers, for which the cross-section radius is $r_0 = 15$ mm, the cross-section opening angle is $\alpha = 16$ deg, and the flat electrode length is $w_e = 13$ mm. The electrostatic rib width is $b = 25$ mm and its length is $l_0 = 130$ mm. Such an electrostatic rib prototype is shown in Figure 10a. The laminate employed in these structures is similar to the one described in Section **??** except that the insulating polyimide layer (cell innermost ply) does not extend to the web region (in which the two GFRP plies meet). An additional layer of polyimide tape is added to the flat electrode region, and wraps around the entire structure providing a full encapsulation against arcing. Finally, flexible conductive tape stripes covered in polyimide connect the cells in series through a hole in the glass fiber and polyimide plies.

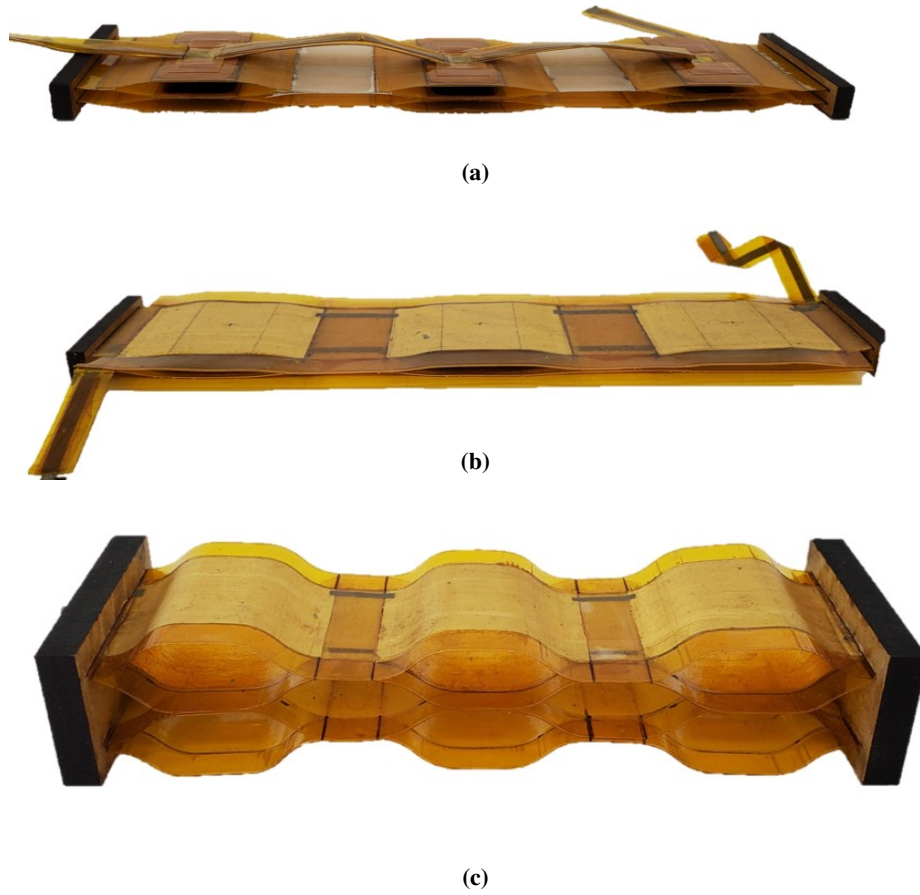**(a)**

(b)

(c)

Fig. 9   (a) Parallel electrode bilayer prototype with $r_0 = 15$ mm and $\alpha_0 = 16$ deg. (b) Zipper electrode bilayer prototype with $r_0 = 15$ mm and $\alpha_0 = 60$ deg. (c) Zipper electrode bilayer prototype with $r_0 = 7$ mm and $\alpha_0 = 60$ deg.

The voltage between electrodes is ramped from 0 to 15 kV at a rate of 1.5 kV/s, and the central rib deflection is measured. The results of these 8 experiments are shown in Figure 10a. We observe that over the whole range of experiments, 6 structures (labeled S3 to S8) exhibit a similar behavior. For this subset of experiments, we compute the average deflection and standard deviation, shown in black and grey respectively in Figure 10a. For the rest of this section, we will refer to this particular behavior as the "stiff regime" (see Figure 11). In addition, 2 structures (S1 and S2) display a significantly different behavior, shown with circles and crosses in Figure 10a. We will refer to this behavior as the "soft regime" (see Figure 11). Finally, the finite element framework described in Section III.A is used to replicate the experiment, and is shown in dashed line in Figure 10a.

We first notice that for all 8 structures, the deflection vs voltage curve is quadratic which agrees with the inverse proportionality between the electrostatic force and the square of the gap distance between electrodes. However, at a critical voltage between 6.5 and 7.5 kV, the quadratic growth in deflection is abruptly interrupted, and the response for a higher range of voltages plateaus or increase very slowly. This type of behavior was observed in other electrostatic actuators[16] and is most likely caused by undesired charging issues. At higher voltages, the electric field is large enough to ionize the air in the cells, and charges deposit on the surface of the polyimide layer through corona discharge. The resulting surface charging effect is referred to as an electrostatic tribolayer [16]. The charges that deposit on one electrode insulation layer have an opposite polarity to that of the electrode, effectively reducing the electric field in the cavity. In addition, the insulation layers for the top and bottom electrodes being so close to each other (even touching in some cases), charges can migrate between these two layers through arcing, which could explain the clicking noise heard during the experiments after the critical voltage is exceeded.
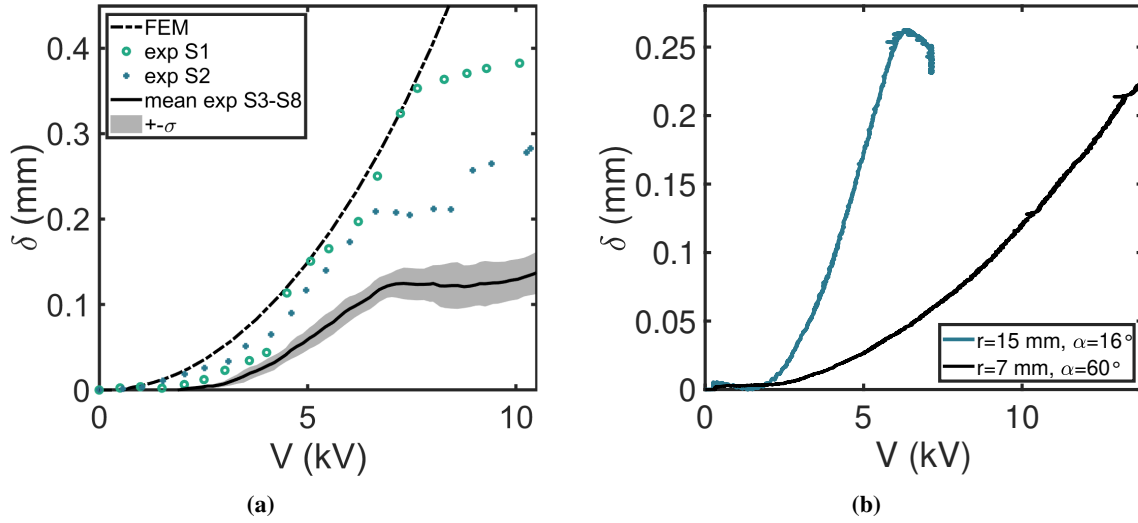
Fig. 10 **(a) Results of 8 tests on parallel electrode prototypes with** $r_0 = 15$ **mm and** $\alpha_0 = 16$ **deg. (b) Results two tests on zipper electrode prototypes.**

The second main observation is the significant difference in behavior between the stiff and soft regimes, even if the 8 structures are nominally identical. The finite element simulation captures well the soft regime, up to the appearance of the electrostatic tribolayer. One promising explanation for this difference in behavior is the presence of geometric imperfections in the top layer cross-section, in particular initial curvature on the upper flat sections of the top cells. When the electrostatic rib undergoes bending, the top layer and therefore the top flat sections, undergo compression. Under this in-plane compressive loading, these nominally planar shells buckle, and postbuckling bending deflection can develop in two possible directions, upward or downward. As such these flat sections are in a bistable state. In practice, initial curvature in the flat sections bias the structures towards following a specific direction of postbuckling deflections. In the case of an initial downward curvature imperfection, compression on the top cells results in downward bending of the flat sections, and the height of the cell decreases. It created a region of high localized curvature at the center of the flat sections, and in opposite directions to the curvature in the circular flanges. This mode of deformation leads to a stiffer structure. In the case of an initial upward curvature imperfection, compression results in upward bending of the flat sections, and the height of the top cell increases. The curvature at the center of the flat section is moderate and in the same direction as the curvature in the circular flanges. This mode of deformation leads to a softer structure. The different deformation mechanisms in the soft and stiff regimes are illustrated in Figure 11. When looking closely at the manufactured structures, we notice that most of them exhibit a small downward initial curvature imperfection on the top layer cells, which seems to agree with our experimental observations. In addition, a sudden increase in deflection is observed for structure S1 at a voltage of 4.25 kV, and this snap-through from the stiff regime to the soft regime supports the bistability hypothesis. A thorough experimental verification of this hypothesis through shape measurement and buckling simulations will be presented in future work. Note that this effect can be mitigated by introducing dominant defects in the nominally flat top cell sections during manufacturing. This approach can also be used to tailor the response of the structures to either produce large deflections (soft regime) or large bending moments (stiff regime).
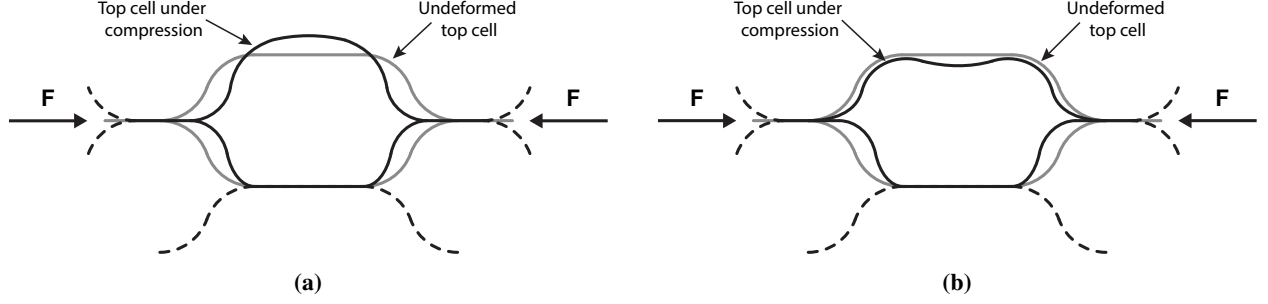
Fig. 11   Top cell deformation mechanism for the (a) soft regime and (b) stiff regime.

In addition to the parallel electrode structures, two zipper electrode prototypes are manufactured and tested. The first one (shallow zipper) features the same geometry as structures S1 to S8, i.e. $r_0 = 15$ mm and $\alpha_0 = 16$ deg. The second structure (tall zipper) features a significantly taller cell cross-section, with a radius $r_0 = 7$ mm and and opening angle $\alpha_0 = 60$ deg. Both zipper prototypes use a GFRP / Kapton laminate similar to the one described in Section III.A, except that the copper foil is replaced by a 3 μm thick gold foil over the entire open cell region. Moreover, the polyimide layer is wider than the glass fiber ply and electrodes to provide protection against arcing. These extra polyimide "wings" do not participate to the overall bending stiffness of the laminate. Finally, conductive tape is integrated between the GFRP and Kapton plies to connect the electrodes.

The results of these two experiments are shown in Figure 10b. The shallow zipper shows a steeper increase in deflection compared to the parallel electrode structures. For an applied voltage of 6 kV, the zipper structure produces a central deflection of $\delta = 0.25$ mm as opposed to about 0.2 mm for the parallel electrode. At a critical voltage of 6.3 kV, an electrostatic tribolayer forms on the polyimide insulation which abruptly stops the increase in deflection. Finally the tall zipper exhibits a much more gradual increase in deflection, than the parallel electrode structures and shallow zipper, and require twice as much voltage as the parallel electrodes to produce comparable deflections. However, the tall zipper exhibits a quadratic increase in deflection even for higher voltages. A change of regime is observed at a voltage of 13.3 kV, which may also be explained by the formation of an electrostatic tribolayer. Since the cross-section is taller, the average electric field strength in the cells is reduced, which delays the generalized breakdown of the air and delay the appearance of the polyimide surface charging. Comparing the zipper experiments with an updated finite element model will be the subject of future work.

VI. Towards Large Scale Surface Shape Control

One of the goals of the research presented in this paper is to eventually use electrostatically actuated thin-shell structures for the shape control of large scale surfaces [17, 23], in applications where limiting the mass of the system is critical. As a proof of concept, the finite element framework described in Section III.A is used to conduct preliminary studies to assess the actuation capabilities of electrostatic lattices. In the simulation, these lattices are made of parallel electrode ribs featuring the same cross-section geometry as the one shown in Figure 9a. Each rib layer has 4 cells and its length is $l_0 = 170$ mm. Figure 12a shows the simulation results of a square lattice morphing into a spherical cap and Figure 12b shows the evolution of the radius of curvature as a function of applied voltage. Note that if cells are individually addressable, this type of architecture can achieve multiple target shapes (saddle, cylinder). Finally, we are interested in actuating these electrostatic structures past the pull-in instability, and one promising avenue of research is the use of bistable cell cross-sections which would be able to lock in their deformed shape even after the voltage between electrodes is removed.
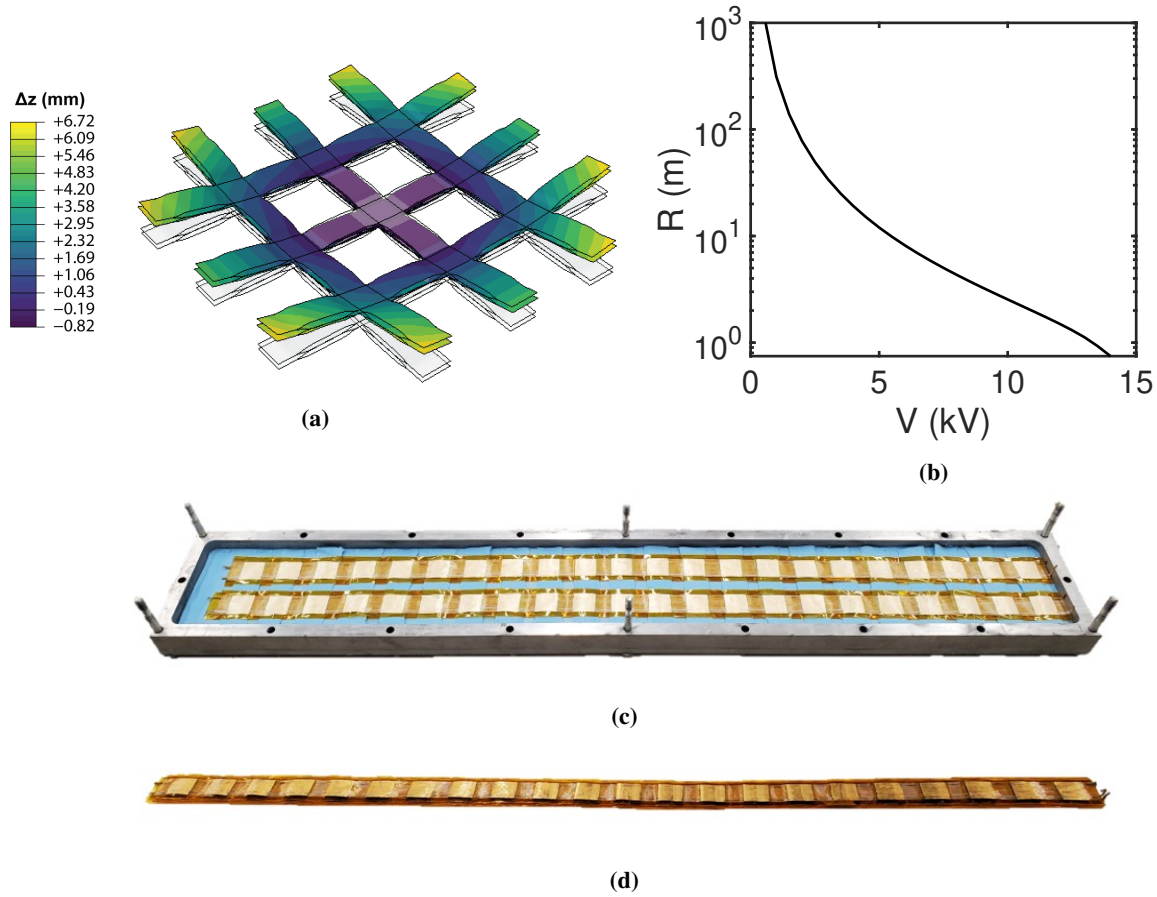
12

Fig. 12 **(a) Simulated deformed shape for a square 3 x 3 lattice morphing into a spherical cap. The deflections have been magnified by a factor of 2, but their magnitude is accurately represented by the color map. (b) Evolution of the spherical cap radius of curvature as a function of applied voltage. (c) 1 m long silicone mold used to create a (d) 900 mm long zipper electrode rib.**

The manufacturing process has been scaled up to create longer electrostatic thin shell structures and large lattices. To create the 1 m long silicone mold shown in Figure 12, a foam mold negative is machined by a hot wire foam cutter, and replaces the 3D printer part discussed in Section III.B. This long mold has successfully been used to create the zipper electrode structure shown in Figure 12, which features the same cross-section geometry as the one shown in Figure 9b.

VII. Conclusion

This paper has presented a novel concept for creating active structures capable of forming large surfaces for which the shape can be adjusted in real time. The concept uses thin-shell cell structures in which conductive electrodes are embedded, and the cell expansion can be controlled by applying a voltage between electrodes. When these cells are arranged into bilayer structures, differential cell expansion is used to generate global structural bending. Two electrode configurations were considered: parallel electrodes and zipper electrodes.

We first developed a novel finite element framework which captures the highly non-linear mechanics of the electrostatic cells. This simulation tool was then used to conduct parametric studies to assess the actuation capabilities these active structures. The study of a single cell for both simply supported and clamped boundary conditions revealed optimal geometries in terms of maximum expansion and reaction force. Moreover, the study of a bilayer cell system showed that these structures can generate significant rotations and reaction moments. We then built several electrostatic thin-shell bilayer structures using a recently developed silicone molding composite manufacturing process. We tested short (130 mm) parallel electrode prototypes and showed that they were able to generate central bending deflections around 200μ m for an applied voltage of 6 kV. The experimental study also revealed a complex charging behavior

13

(electrostatic tribolayer) which was limiting the amount of bending deflection at higher voltages. Moreover, the experiment showed that the chosen cell cross-section was imperfection sensitive, leading to a soft and stiff bending regime. The soft bending regime was captured accurately by the finite element model but additional work is required to replicate the stiff regime in simulation. Furthermore, we tested two prototypes featuring zipper electrodes, which have shown superior bending capabilities compared to the parallel electrode structures and are therefore the most promising types of structures for the shape control of large systems. This experiment paves the way to the integration of electrostatic thin shell ribs into large planar lattices. The ability of such lattices to morph into 3D shapes has been shown through a finite element simulation, and we presented a pathway to manufacture them using larger molds.

The work presented in this paper can serve as a proof of concept from which more complex systems can be engineered. The research focused on quasi-static voltage actuation, but the dynamic actuation and real time shape control of these systems is important to investigate. The use of the electrodes as capacitive shape sensors is a potential avenue for the design of a fully integrated curvature control solution. On the electrical side, detrimental charging effects can be mitigated by engineering new laminates and provide a pathway to operating these structures at higher voltages. Higher dielectric liquid layers could also be employed to maximize actuation capabilities at low voltages[24]. Finally, bistability in the cell cross-sections can be used to shape lattices into 3D structures without requiring continuous actuation. The electrostatic actuation would only be applied for the structure to switch between the undeformed and deformed stable states.

VIII. Acknowledgements

References

[1] E. N. Stavros, S. E. O., C. E. Jones, "NISAR Utilization Plan, NASA JPL D-102207," 2018.

[2] Arya, M., Lee, N., and Pellegrino, S., *Ultralight Structures for Space Solar Power Satellites*, 2016. https://doi.org/10.2514/6.2016-1950.

[3] Brophy, J., Pellegrino, S., Lubin, P., Alkalai, L., Atwater, H., Biswas, A., Boca, A., Carr, G., Davoyan, A., Frazier, W., et al., "Non-Nuclear Exploration of the Solar System Study," 2022.

[4] Fernandez, J. M., Rose, G., Stohlman, O. R., Younger, C. J., Dean, G. D., Warren, J. E., Kang, J. H., Bryant, R. G., and Wilkie, K. W., *An Advanced Composites-Based Solar Sail System for Interplanetary Small Satellite Missions*, 2018. https://doi.org/10.2514/6.2018-1437.

[5] Bolcar, M. R., Balasubramanian, K., Clampin, M., Crooke, J., Feinberg, L., Postman, M., Quijada, M., Rauscher, B., Redding, D., Rioux, N., Shaklan, S., Stahl, H. P., Stahle, C., and Jr., H. T., "Technology development for the Advanced Technology Large Aperture Space Telescope (ATLAST) as a candidate large UV-Optical-Infrared (LUVOIR) surveyor," *UV/Optical/IR Space Telescopes and Instruments: Innovative Technologies and Concepts VII*, Vol. 9602, edited by H. A. MacEwen and J. B. Breckinridge, International Society for Optics and Photonics, SPIE, 2015, pp. 86 – 99. https://doi.org/10.1117/12.2188559, URL https://doi.org/10.1117/12.2188559.

[6] Hedgepeth, J., *Critical requirements for the design of large space structures*, 1981. https://doi.org/10.2514/6.1981-443, URL https://arc.aiaa.org/doi/abs/10.2514/6.1981-443.

[7] Banik, J., "Realizing large structures in space," *Proc., Frontiers of Engineering: Reports on Leading-Edge Engineering from the 2015 Symp*, 2016, pp. 55–62.

[8] Lake, M., Levine, M., and Peterson, L., "Rationale for Defining Structural Requirements for Large Space Telescopes," *Journal of Spacecraft and Rockets - J SPACECRAFT ROCKET*, Vol. 39, 2002, pp. 674–681. https://doi.org/10.2514/2.3889.

[9] Acton, D. S., Knight, J. S., Contos, A., Grimaldi, S., Terry, J., Lightsey, P., Barto, A., League, B., Dean, B., Smith, J. S., Bowers, C., Aronstein, D., Feinberg, L., Hayden, W., Comeau, T., Soummer, R., Elliott, E., Perrin, M., and Jr., C. W. S., "Wavefront sensing and controls for the James Webb Space Telescope," *Space Telescopes and Instrumentation 2012: Optical, Infrared, and Millimeter Wave*, Vol. 8442, International Society for Optics and Photonics, SPIE, 2012, p. 84422H. https://doi.org/10.1117/12.925015.

[10] Steeves, J., Laslandes, M., Pellegrino, S., Redding, D., Bradford, S. C., Wallace, J. K., and Barbee, T., "Design, fabrication and testing of active carbon shell mirrors for space telescope applications," *Advances in Optical and Mechanical Technologies for Telescopes and Instrumentation*, Vol. 9151, edited by R. Navarro, C. R. Cunningham, and A. A. Barto, International Society for Optics and Photonics, SPIE, 2014, pp. 33 – 45. https://doi.org/10.1117/12.2056560, URL https://doi.org/10.1117/12.2056560.

[11] Li, J., Brenner, M., Christen, T., Kotilainen, M., Lang, J., and Slocum, A., "Deep-reactive ion-etched compliant starting zone electrostatic zipping actuators," *Journal of Microelectromechanical Systems*, Vol. 14, No. 6, 2005, pp. 1283–1297. https://doi.org/10.1109/JMEMS.2005.851842.

[12] Ito, M., and Saneyoshi, K., "Development of large-scale stacked-type electrostatic actuators for use as artificial muscles," *Advanced Robotics*, Vol. 28, No. 11, 2014, pp. 759–767. https://doi.org/10.1080/01691864.2013.867289.

[13] Kellaris, N., Venkata, V. G., Smith, G. M., Mitchell, S. K., and Keplinger, C., "Peano-HASEL actuators: Muscle-mimetic, electrohydraulic transducers that linearly contract on activation," *Science Robotics*, Vol. 3, No. 14, 2018, p. eaar3276. https://doi.org/10.1126/scirobotics.aar3276.

[14] Lang, J. H., and Staelin, D. H., "Electrostatically-controlled large-aperture reflecting satellite antennas," *1980 19th IEEE Conference on Decision and Control including the Symposium on Adaptive Processes*, 1980, pp. 991–993. https://doi.org/10.1109/CDC.1980.271950.

[15] Bhundiya, H. G., Zhang, J. Z., Overby, K. D., Royer, F., Lang, J. H., Cordero, Z. C., Moulder, W. F., Jeon, S. K., and Silver, M. J., *Electrostatically Actuated X-Band Mesh Reflector with Bend-Formed Support Structure*, 2023.

[16] Horenstein, M. N., Bifano, T. G., Mali, R. K., and Vandelli, N., "Electrostatic effects in micromachined actuators for adaptive optics," *Journal of Electrostatics*, Vol. 42, No. 1, 1997, pp. 69–81. https://doi.org/https://doi.org/10.1016/S0304-3886(97)00138-1.

[17] Liu, K., Hacker, F., and Daraio, C., "Robotic surfaces with reversible, spatiotemporal control for shape morphing and object manipulation," *Science Robotics*, Vol. 6, No. 53, 2021, p. eabf5116. https://doi.org/10.1126/scirobotics.abf5116.

[18] Risso, G., Sakovsky, M., and Ermanni, P., "A Highly Multi-Stable Meta-Structure via Anisotropy for Large and Reversible Shape Transformation," *Advanced Science*, Vol. 9, No. 26, 2022, p. 2202740. https://doi.org/https://doi.org/10.1002/advs.202202740.

[19] Fernandez, J., "Advanced Deployable Shell-Based Composite Booms for Small Satellite Structural Applications Including Solar Sails," *4th International Symposium on Solar, Kyoto, Japan*, 2017.

[20] Royer, F., and Pellegrino, S., *Ultralight Ladder-type Coilable Space Structures*, 2018. https://doi.org/10.2514/6.2018-1200, URL https://arc.aiaa.org/doi/abs/10.2514/6.2018-1200.

[21] Schlothauer, A., Royer, F., Pellegrino, S., and Ermanni, P., "Flexible Silicone Molds For the Rapid Manufacturing of Ultra-Thin Fiber Reinforced Structures," 2018.

[22] *PMT-F7 Technical datasheet*, Patz Materials and Technologies, 2022.

[23] Boley, J. W., van Rees, W. M., Lissandrello, C., Horenstein, M. N., Truby, R. L., Kotikian, A., Lewis, J. A., and Mahadevan, L., "Shape-shifting structured lattices via multimaterial 4D printing," *Proceedings of the National Academy of Sciences*, Vol. 116, No. 42, 2019, pp. 20856–20862. https://doi.org/10.1073/pnas.1908806116.

[24] Taghavi, M., Helps, T., and Rossiter, J., "Electro-ribbon actuators and electro-origami robots," *Science Robotics*, Vol. 3, No. 25, 2018, p. eaau9795. https://doi.org/10.1126/scirobotics.aau9795.